INTERNATIONAL JOURNAL FOR NUMERICAL METHODS IN FLUIDS
Int. J. Numer. Meth. Fluids 2001; **37**: 905–931 (DOI: 10.1002/fld.196)

Numerical simulation of the unsteady flow over an elliptic cylinder at different orientations

H. M. Badr[a,*], S. C. R. Dennis[b] and Serpil Kocabiyik[c]

[a] *Mechanical Engineering Department, King Fahd University of Petroleum and Minerals, Dhahran, Saudi Arabia*
[b] *Department of Applied Mathematics, The University of Western Ontario, London, Ontario, Canada*
[c] *Department of Mathematics and Statistics, Memorial University of Newfoundland, St. John's, Newfoundland, Canada*

SUMMARY

A numerical method is developed for investigating the two-dimensional unsteady viscous flow over an inclined elliptic cylinder placed in a uniform stream of infinite extent. The direction of the free stream is normal to the cylinder axis and the flow field unsteadiness arises from two effects, the first is due to the flow field development following the start of the motion and the second is due to vortex shedding in the wake region. The time-dependent flow is governed by the full conservation equations of mass and momentum with no boundary layer approximations. The parameters involved are the cylinder axis ratio, Reynolds number and the angle of attack. The investigation covers a Reynolds number range up to 5000. The minor–major axis ratio of the elliptic cylinder ranges between 0.5 and 0.6, and the angle of attack ranges between 0° and 90°. A series truncation method based on Fourier series is used to reduce the governing Navier–Stokes equations to two coupled infinite sets of second-order differential equations. These equations are approximated by retaining only a finite number of terms and are then solved by approximating the derivatives using central differences. The results reveal an unusual phenomenon of negative lift occurring shortly after the start of motion. Various comparisons are made with previous theoretical and experimental results, including flow visualizations, to validate the solution methodology.

KEY WORDS: different orientations; elliptic cylinder; numerical simulation; unsteady flow

1. INTRODUCTION

This paper considers the classical problem of unsteady two-dimensional uniform flow past an impulsively started inclined elliptic cylinder. The initial development of this flow was investigated by Wang [1], Dennis and Staniforth [2], Staniforth [3] and Panniker and Lavan [4]. All of these studies were carried out at high but finite values of the Reynolds number, except for

* Correspondence to: Mechanical Engineering Department, King Fahd University of Petroleum and Minerals, KFUPM Box # 322, Dhahran 31261, Saudi Arabia.

Received 22 May 2000
Revised 5 February 2001

Panniker and Lavan in which the initial flow was investigated at a Reynolds number of 200. It is well known that the early development of the flow after the start can be determined analytically using the method of inner and outer expansions by taking the interactions between the boundary layer and the outer inviscid flow into consideration. Wang [1] adopted this approach to obtain uniformly valid solutions throughout the flow field with emphasis on separation and stall. He found that the lift continuously increases from an initial value of zero, contrary to the view put forward by Howarth [5] that no lift occurs up to the time of separation. Staniforth [3, pp. 21–33], on the other hand, worked out the underlying basic structure of the initial flow by analysis, but with only the inner solutions determined using global integral conditions on the vorticity without the necessity of finding the outer solutions, often of lesser interest from a practical point of view. It is noted that complete details of the matching procedure can be established using integral conditions that can be derived from one of Green's identities and the details of the outer solution can be given if desired (see Dennis and Kocabiyik [6] for further explanation of these conditions). In Staniforth's work, numerical solutions to the same problem were also determined numerically utilizing initial boundary layer structure of the flow and a spatial transformation that stretches with the increase of time. Although Staniforth's solution is highly accurate, its validity is limited to high Reynolds numbers and small times. Panniker and Lavan [4] calculated the initial flow for viscous incompressible flow over an impulsively started ellipse numerically at an angle of attack of 20° using both the Green's function method and finite differences in the case of a Reynolds number of 200.

Numerical solutions of laminar flow past elliptic cylinders at various angles of attack were obtained by Lugt and Haussling [7], who studied the problem of flow development past an abruptly accelerated elliptic cylinder at 45° incidence in the range of Reynolds numbers from 15 to 200. Comparisons between the obtained location of the first vortex and the flow visualization results reported by Honji [8] show good agreement. However, the surface pressure distribution reported in Lugt and Haussling's paper shows some discrepancies since the pressure periodicity is not fully satisfied ($P_0 \neq P_{2\pi}$). The numerical solutions to the uniform flow over an inclined elliptic cylinder were determined for moderate and large values of the time by Patel [9] and later by Nair and Sengupta [10]. Patel obtained a numerical solution in the range of Reynolds numbers from 60 to 200. Patel's solution is based on a Fourier series approximation of streamfunction and vorticity. In the work of Nair and Sengupta, the incompressible flow past impulsively started elliptic cylinders of aspect ratio of 0.1 and 0.25 was computed for Reynolds number of 3000 and 10^4. Navier–Stokes equations were solved in their streamfunction–vorticity formulation using a two-dimensional direct numerical simulation. In these numerical studies, a potential flow solution was used as an initial condition at the start of the cylinder motion and also no measures were taken to ensure the periodicity of pressure.

Experimental studies of the uniform flow over inclined elliptic cylinders were carried out by Honji [8] and Taneda [11,12]. Honji [8] observed the starting flow around a sphere and an elliptic cylinder at 45° and 54° angles of incidences. Taneda [11] studied the relationship between lift and flow pattern for the case of an impulsively started elliptic cylinder at angles of incidence of 20° and 45° in the cases of Reynolds numbers 3500 and 6000 respectively. He reported very high initial lift values and a gradual downward movement of the rear stagnation

point. In addition, it was pointed out that lift takes negative values in a small time interval shortly after the impulsive start in the case of angle of attack 20° unlike the case of angle of attack 45°. One of the most comprehensive experimental works on unsteady separated flows around bodies is that of Taneda [12]. He studied flow patterns around two-dimensional bodies like circular and elliptic cylinders, flat plates and flexible plates. The unsteady motions studied were the impulsive start from rest, change of velocity, translational oscillation, change of angle of incidence, uniform rotation, rotational oscillation and swimming motion. In the case of uniform flow past an impulsively started inclined elliptic cylinder, he again reported that the negative lift occurs shortly after the start of motion depending upon the value of the angle of inclination.

In this paper, the problem of uniform flow past an impulsively started inclined elliptic cylinder is considered. The problem is solved for Reynolds numbers ranging from 900 to 5000 and for the range of angle of attack between 0 and 90°. The method of solution, which is based on a numerical integration of the Navier–Stokes equations, is verified by applying it to problems of known numerical or experimental solutions. Laminar flow assumption is made and the cylinder axis ratio is assumed to be 0.5 or 0.6. The time variation of the flow field is presented in the form of streamline patterns as well as surface vorticity distribution. The surface pressure distribution and the time variation of the drag and lift force coefficients are also calculated. It is found that an unusual behavior in the lift coefficient, not reported in previous numerical studies, occurs depending upon the value of the angle of inclination and is consistent with the experimental findings of Taneda [11,12]. The results of this study are of theoretical and practical importance, since it adds to the knowledge of fluid force coefficients and is directly related to several engineering applications.

2. GOVERNING EQUATIONS AND METHOD OF SOLUTION

In the present work we consider the two-dimensional flow caused by an infinitely long elliptic cylinder set in motion impulsively which translates with uniform velocity U in the horizontal direction. The cylinder is assumed to be inclined to the horizontal direction at an angle α. The ellipse has major and minor axis of lengths $2a$ and $2b$ respectively. Using the Cartesian co-ordinate system shown in Figure 1, the Navier–Stokes equations and the mass conservation equation can be expressed in the form of Helmholtz vorticity transport equation and stream function equation as

$$\frac{\partial \zeta}{\partial t} + u\frac{\partial \zeta}{\partial x} + v\frac{\partial \zeta}{\partial y} = \frac{2}{Re}\left(\frac{\partial^2 \zeta}{\partial x^2} + \frac{\partial^2 \zeta}{\partial y^2}\right) \tag{1}$$

$$\frac{\partial^2 \psi}{\partial x^2} + \frac{\partial^2 \psi}{\partial y^2} = \zeta \tag{2}$$

where x and y are the co-ordinates shown in Figure 1, t is the time, ψ is the streamfunction, ζ is the vorticity, u and v are the velocities in the x- and y-directions, Re is the Reynolds number defined as $Re = U(2c)/v$, and

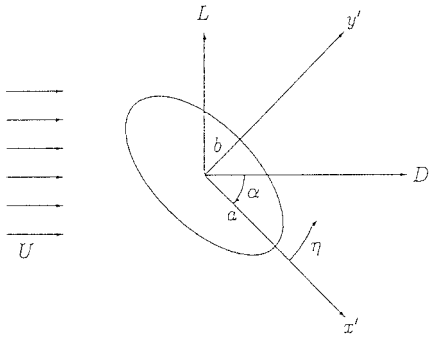

Figure 1. Co-ordinate system and flow configuration.

$$u = \frac{\partial \psi}{\partial y}, \qquad v = -\frac{\partial \psi}{\partial x}$$

All above variables are dimensionless. They are related to the dimensional variables (with primes) by

$$x = \frac{x'}{c}, \qquad y = \frac{y'}{c}, \qquad u = \frac{u'}{U}, \qquad v = \frac{v'}{U}, \qquad t = \frac{Ut'}{c}, \qquad \psi = \frac{\psi'}{cU}, \qquad \zeta = -\frac{\zeta' c}{U}$$

where c stands for the focal distance of the ellipse defined by $c = \sqrt{a^2 - b^2}$. The boundary conditions are simply the no-slip and impermeability conditions at the solid surface and the free stream conditions far away from it. It can be represented by

$$\psi = \frac{\partial \psi}{\partial x} = \frac{\partial \psi}{\partial y} = 0 \quad \text{on the cylinder surface} \tag{3a}$$

$$\frac{\partial \psi}{\partial y} \to \cos \alpha, \qquad \frac{\partial \psi}{\partial x} \to -\sin \alpha \quad \text{far away from the surface} \tag{3b}$$

The elliptic co-ordinate system (ξ, η) defined by the transformation

$$x = \cosh \xi \cos \eta, \qquad y = \sinh \xi \sin \eta$$

is used with the origin at the center of the cylinder. The governing equations in the elliptic co-ordinate system are

$$\frac{\partial^2 \psi}{\partial \xi^2} + \frac{\partial^2 \psi}{\partial \eta^2} = H\zeta \tag{4}$$

$$H\frac{\partial\zeta}{\partial t}+\left(\frac{\partial\psi}{\partial\eta}\frac{\partial\zeta}{\partial\xi}-\frac{\partial\psi}{\partial\xi}\frac{\partial\zeta}{\partial\eta}\right)=\frac{2}{Re}\left(\frac{\partial^2\zeta}{\partial\xi^2}+\frac{\partial^2\zeta}{\partial\eta^2}\right) \tag{5}$$

where

$$H=\frac{1}{2}[\cosh(2\xi)-\cos(2\eta)]$$

The boundary conditions given in Equation (3) can be expressed in the new co-ordinate system as

$$\psi=\frac{\partial\psi}{\partial\xi}=\frac{\partial\psi}{\partial\eta}=0 \quad \text{when } \xi=\xi_0 \tag{6a}$$

$$\frac{\partial\psi}{\partial\xi}\to\frac{1}{2}e^{\xi}\sin(\eta-\alpha) \quad \text{as } \xi\to\infty \tag{6b}$$

$$\frac{\partial\psi}{\partial\eta}\to\frac{1}{2}e^{\xi}\cos(\eta-\alpha) \quad \text{as } \xi\to\infty \tag{6c}$$

Here the constant ξ_0 is defined by $\xi_0=\tanh^{-1}(\bar{r})$, where $\bar{r}$ is the aspect ratio of ellipse defined by $\bar{r}=b/a$ and $\xi=\xi_0$ defines the surface of the cylinder.

The Navier–Stokes equations (4) and (5) are solved by finite differences using a Crank–Nicolson iterative procedure with under-relaxation applied only to the surface vorticity. The method is based on approximating the stream function and the vorticity using Fourier series expansion. The method is essentially a generalization of that used by Badr and Dennis [13] and Badr *et al.* [14] in which the functions ψ and ζ were expressed in the form of Fourier series

$$\psi=\frac{1}{2}F_0(\xi,t)+\sum_{n=1}^{N}f_n(\xi,t)\sin n\eta+F_n(\xi,t)\cos n\eta \tag{7a}$$

$$\zeta=\frac{1}{2}G_0(\xi,t)+\sum_{n=1}^{N}g_n(\xi,t)\sin n\eta+G_n(\xi,t)\cos n\eta \tag{7b}$$

In the case of $\alpha=0°$, the functions $F_n(\xi,t)$ and $G_n(\xi,t)$ are identically zero in Equations (7), whereas in the case of $\alpha=90°$, the functions $f_{2p-1}(\xi,t)$, $F_{2p}(\xi,t)$, $g_{2p-1}(\xi,t)$, $G_{2p}(\xi,t)$ for all integers $p\geq 1$ are identically zero in Equation (7). This is due to the fact that in the first the flow is symmetric about $\eta=0$ and in the second the flow is symmetric about $\eta=90°$. The equations governing the functions in Equations (7a) and (7b) can be obtained by substitution into Equations (4) and (5) and then integration of the resulting equation, after multiplication of each side at a time by $\{1,\cos n\eta,\sin n\eta: n=1,2,\ldots\}$ with respect to η from 0 to 2π, it is found that

$$\frac{\partial^2 F_0}{\partial \xi^2} = \frac{1}{2}(\cosh 2\xi) G_0 - \frac{1}{2} G_2 \tag{8a}$$

$$\frac{\partial^2 F_n}{\partial \xi^2} - n^2 F_n = \frac{1}{2}(\cosh 2\xi) G_n - \frac{1}{4}[G_0 \delta_{n2} + G_{|n-2|} + G_{(n+2)}] \tag{8b}$$

$$\frac{\partial^2 f_n}{\partial \xi^2} - n^2 f_n = \frac{1}{2}(\cosh 2\xi) g_n - \frac{1}{4}[\mathrm{sgn}(n-2) g_{|n-2|} + g_{(n+2)}] \tag{8c}$$

$$\frac{1}{2}(\cosh 2\xi)\frac{\partial G_0}{\partial t} - \frac{1}{2}\frac{\partial G_2}{\partial t} = \left(\frac{2}{Re}\right)\frac{\partial^2 G_0}{\partial \xi^2} + S_{n0}(\xi, t) \tag{9a}$$

$$\begin{aligned}&(\cosh 2\xi)\frac{\partial G_n}{\partial t} - \frac{1}{2}\left[\frac{\partial G_0}{\partial t}\delta_{n2} + \frac{\partial G_{|n-2|}}{\partial t} + \frac{\partial G_{n+2}}{\partial t}\right] \\ &= \frac{4}{Re}\left[\frac{\partial G_n}{\partial \xi^2} - n^2 G_n\right] + n g_n \frac{\partial F_0}{\partial \xi} - n f_n \frac{\partial G_0}{\partial \xi} + S_{n1}(\xi, t)\end{aligned} \tag{9b}$$

$$\begin{aligned}&(\cosh 2\xi)\frac{\partial g_n}{\partial t} - \frac{1}{2}\mathrm{sgn}(n-2)\frac{\partial g_{|n-2|}}{\partial t} - \frac{1}{2}\frac{\partial g_{n+2}}{\partial t} \\ &= \frac{4}{Re}\left[\frac{\partial^2 g_n}{\partial \xi^2} - n^2 g_n\right] + n F_n \frac{\partial G_0}{\partial \xi} - n G_n \frac{\partial F_0}{\partial \xi} + S_{n2}(\xi, t)\end{aligned} \tag{9c}$$

where

$$s_{n0} = \sum_{n=1}^{\infty} \frac{\partial}{\partial \xi}[n(F_n g_n - f_n G_n)] \tag{10a}$$

$$\begin{aligned}s_{n1} = \sum_{m=1}^{\infty} \Bigg[&((m-n)F_j + kF_k)\frac{\partial g_m}{\partial \xi} - (jf_j + kf_k)\frac{\partial G_m}{\partial \xi} + m\left(\frac{\partial F_j}{\partial \xi} + \frac{\partial F_k}{\partial \xi}\right) g_m \\ &- m\left(\mathrm{sgn}(m-n)\frac{\partial f_j}{\partial \xi} + \frac{\partial f_k}{\partial \xi}\right) G_m\Bigg]\end{aligned} \tag{10b}$$

$$\begin{aligned}s_{n2} = \sum_{m=1}^{\infty} \Bigg[&(kf_k - jf_j)\frac{\partial g_m}{\partial \xi} - ((m-n)F_j - kF_k)\frac{\partial G_m}{\partial \xi} - m\left(\frac{\partial F_j}{\partial \xi} - \frac{\partial F_k}{\partial \xi}\right) G_m \\ &- m\left(\mathrm{sgn}(m-n)\frac{\partial f_j}{\partial \xi} - \frac{\partial f_k}{\partial \xi}\right) g_m\Bigg]\end{aligned} \tag{10c}$$

Here δ_{mn} is the Kronecker delta symbol defined by

$$\delta_{mn} = 1 \quad \text{if } m = n, \qquad \delta_{mn} = 0, \quad \text{if } m \neq n$$

and $\mathrm{sgn}(m-n)$ is the sign of $(m-n)$ with $\mathrm{sgn}(0)=0$. Equations (8a)–(8c) and (9a)–(9c) define two sets of $(2N+1)$ partial differential equations to be solved, where N is the order of truncation in the Fourier series.

The boundary conditions for all the functions given in Equations (8) and (9) can be obtained using Equations (6) and (7), which results in the following:

$$F_0 = \frac{\partial F_0}{\partial \xi} = f_n = \frac{\partial f_n}{\partial \xi} = F_n = \frac{\partial F_n}{\partial \xi} = 0 \quad \text{when } \xi = \xi_0 \tag{11a}$$

$$G_0,\ g_n,\ G_n \to 0 \quad \text{as } \xi \to \infty \tag{11b}$$

$$F_0 \to 0,\ f_n \to \frac{1}{2}\mathrm{e}^{\xi}\cos(\alpha)\delta_{n1} \quad \text{as } \xi \to \infty \tag{11c}$$

$$F_n \to -\frac{1}{2}\mathrm{e}^{\xi}\sin(\alpha)\delta_{n1} \quad \text{as } \xi \to \infty \tag{11d}$$

It may be shown that the conditions (9) and (10) can be combined to give a further set of conditions of global type, namely

$$\int_{\xi_0}^{\infty} \{(\cosh 2\xi)G_0 - G_2\}\,\mathrm{d}\xi = 0 \tag{12a}$$

$$\int_{\xi_0}^{\infty} \left\{\frac{1}{2}(\cosh 2\xi)G_n - \frac{1}{4}(G_0\delta_{n2} + G_{|n-2|} + G_{n+2})\right\}\mathrm{e}^{-n\xi}\,\mathrm{d}\xi = -\sin\alpha\delta_{n1} \tag{12b}$$

$$\int_{\xi_o}^{\infty} \left\{\frac{1}{2}(\cosh 2\xi)g_n - \frac{1}{4}(\mathrm{sgn}(n-2)g_{|n-2|} + g_{n+2})\right\}\mathrm{e}^{-n\xi}\,\mathrm{d}\xi = \cos\alpha\delta_{n1} \tag{12c}$$

These integral conditions are used to calculate the values of functions g_n and G_n on the cylinder surface at every time step. The first condition (12a) is essential for ensuring that the pressure is single valued at any point around the cylinder surface. It is important here to mention that the issue of periodicity of pressure was raised, but not resolved, in the work by Pannikar and Lavan [4]. The numerical scheme used for advancing the solution of ψ and ζ through one time step is essentially the same as that given by Badr and Dennis [13]. The only difference is the appearance of the derivatives $\partial G_2/\partial t$ in Equation (9a), $(\partial G_{|n-2|}/\partial t,\ \partial G_{n+2}/\partial t)$ in Equation (9b), and $(\partial G_0/\partial t,\ \partial g_{|n-2|}/\partial t,\ \partial g_{n+2}/\partial t)$ in Equation (9c). When solving for g_n or G_n, the functions with subscripts $(n+2)$ are unknown. These unknown functions $(\partial g_{n+2}/\partial t,\ \partial G_{n+2}/\partial t)$ were taken care of by approximating their values at time $(t+\Delta t)$ to be initially the same as at time t and then updating these values through an iterative procedure.

In order to start the integration scheme, an initial solution for the governing equations at $t=0$ must be known. Equations (8) and (9) determine the development of the flow at some time after the impulsive start, but during the initial stages of the motion the boundary layer co-ordinates (x, τ) can be introduced by the transformation

$$\xi = \xi_0 + kx, \quad \text{where } k = 2\sqrt{\frac{2\tau}{R}}, \quad \tau = t \tag{13}$$

This is employed to transform all the appropriate equations with the following scaling of variables:

$$F_n = kF_n^*, \qquad G_n = G_n^*/k, \qquad f_n = kf_n^*, \qquad g_n = g_n^*/k \tag{14}$$

After suppressing all stars, Equations (8a)–(8c) become

$$\frac{\partial^2 F_0}{\partial x^2} = \frac{1}{2}\cosh[2(\xi_0 + kx)]G_0 - \frac{1}{2}G_2 \tag{15a}$$

$$\frac{\partial^2 F_n}{\partial x^2} - n^2k^2F_n = \frac{1}{2}\cosh[2(\xi_0 + kx)]G_n - \frac{1}{4}[G_0\delta_{n2} + G_{|n-2|} + G_{(n+2)}] \tag{15b}$$

$$\frac{\partial^2 f_n}{\partial x^2} - n^2k^2f_n = \frac{1}{2}\cosh[2(\xi_0 + kx)]g_n - \frac{1}{4}[\mathrm{sgn}(n-2)g_{|n-2|} + g_{(n+2)}] \tag{15c}$$

while Equations (9a)–(9c) become

$$\frac{\partial^2 G_0}{\partial x^2} + \cosh[2(\xi_0 + kx)]\left(x\frac{\partial G_0}{\partial x} + G_0\right) = 2\tau\cosh[2(\xi_0 + kx)]\frac{\partial G_0}{\partial \tau} - 4\tau T_{n0} \tag{16a}$$

$$\begin{aligned}&\frac{\partial^2 G_n}{\partial x^2} + \cosh[2(\xi_0 + kx)]\left(x\frac{\partial G_n}{\partial x} + G_n\right)\\ &= 2\tau\cosh[2(\xi_0 + kx)]\left(\frac{\partial G_n}{\partial \tau}\right) + \frac{8\tau}{R}n^2G_n + 2\tau\left[nf_n\frac{\partial G_0}{\partial x} - ng_n\frac{\partial F_0}{\partial x} - T_{n1}\right]\end{aligned} \tag{16b}$$

$$\begin{aligned}&\frac{\partial^2 g_n}{\partial x^2} + \cosh[2(\xi_0 + kx)]\left(x\frac{\partial g_n}{\partial x} + g_n\right)\\ &= 2\tau\cosh[2(\xi_0 + kx)]\left(\frac{\partial g_n}{\partial \tau}\right) + \frac{8\tau}{R}n^2g_n - 2\tau\left[nF_n\frac{\partial G_0}{\partial x} - nG_n\frac{\partial F_0}{\partial x} + T_{n2}\right]\end{aligned} \tag{16c}$$

where T_{n0}, T_{n1} and T_{n2} are easily identifiable functions of the Fourier coefficients. The boundary and integral conditions simply become

$$F_0 = \frac{\partial F_0}{\partial x} = f_n = \frac{\partial f_n}{\partial x} = F_n = \frac{\partial F_n}{\partial x} = 0 \quad \text{when } x = 0 \tag{17a}$$

$$G_0,\ g_n,\ G_n \to 0 \quad \text{as } x \to \infty \tag{17b}$$

$$kf_n \to \mathrm{e}^{\xi_0}\sinh(kx)\cos(\alpha)\delta_{n1} \quad \text{as } x \to \infty \tag{17c}$$

$$kF_n \to -\mathrm{e}^{\xi_0}\sinh(kx)\sin(\alpha)\delta_{n1} \quad \text{as } x \to \infty \tag{17d}$$

$$\int_{\xi_0}^{\infty} \{[\cosh 2(\xi_0 + kx)]G_0 - G_2\}\,\mathrm{d}x = 0 \tag{18a}$$

$$\int_{\xi_0}^{\infty} \left\{\frac{1}{2}[\cosh 2(\xi_0 + kx)]G_n - \frac{1}{4}(G_0\delta_{n2} + G_{|n-2|} + G_{n+2})\right\}\mathrm{e}^{-nkx}\,\mathrm{d}x = -\mathrm{e}^{\xi_0}\sin\alpha\delta_{n1} \tag{18b}$$

$$\int_{\xi_0}^{\infty} \left\{\frac{1}{2}[\cosh 2(\xi_0 + kx)]g_n - \frac{1}{4}(\mathrm{sgn}(n-2)g_{|n-2|} + g_{n+2})\right\}\mathrm{e}^{-nkx}\,\mathrm{d}x = \mathrm{e}^{\xi_0}\cos\alpha\delta_{n1} \tag{18c}$$

The governing equations and boundary and integral conditions (15)–(18) are solved using a special integrating scheme for (15) similar to that used by Badr and Dennis [13] and a Crank–Nicolson scheme for Equation (16). It is important to mention that the boundary layer co-ordinate x will continuously stretch with time when viewed in the physical co-ordinates. This behavior matches the phenomenon under investigation since the viscous region starts with zero thickness at $\tau = 0$ and grows as time increases.

The initial solution obtained by Staniforth [3] at $\tau = 0$ can be expressed as

$$\psi = \mathrm{e}^{\xi_0}\sin(\eta - \alpha)\left[x\,\mathrm{erf}(H_0^{1/2}x) + \frac{1}{\pi^{1/2}H_0^{1/2}}(\mathrm{e}^{-H_0x^2} - 1)\right] \tag{19a}$$

$$\zeta = \frac{2}{\pi^{1/2}H_0^{1/2}}\mathrm{e}^{\xi_0}\sin(\eta - \alpha)\,\mathrm{e}^{-H_0x^2} \tag{19b}$$

where

$$H_0 = \frac{1}{2}(\cosh 2\xi_0 - \cos 2\eta)$$

The Fourier functions (G_n, g_n, F_n, f_n) corresponding to the initial solution given in Equation (19) are obtained numerically. By trying different numbers of terms, it is found that 15 terms in the Fourier series are sufficient to accurately approximate the above expressions. The use of the initial solution is very essential for obtaining accurate results at small time. The use of a potential solution as an initial condition at $\tau = 0$ was frequently adopted by many researchers; however, this will definitely lead to inaccurate results following the start of fluid motion. The effect of such inaccuracy on the large time results is not known.

The integral conditions (18) are used to calculate the values of the functions G_n, and g_n on the cylinder surface ($\xi = \xi_0$) at every time step. Following the start of fluid motion, very small time steps ($\Delta\tau = 10^{-4}$) are taken since the time variation of the vorticity field is quite fast. However, as time increases, the time step was gradually increased until reaching $\Delta\tau = 0.05$. The number of points in the ξ direction is taken as 101 with a space step of $\Delta\xi = 0.1$. This makes $\xi_{\max} = \xi_0 + 10$, which sets the outer boundary at a physical distance of at least 11000 times the focal distance. Such a far-away boundary ensures that the application of the boundary

conditions (17c) and (17d) does not impose any unrealistic conditions on the solution scheme. The number of terms in the series (7a) and (7b) starts with 15 at $\tau = 0$ and more terms are added as time increases. One more term is added at a time when the last term in the series reaches a maximum value of 10^{-4}. Using numerical experimentation it is found that, for the range of Reynolds number considered in this paper, a maximum of 30 terms is adequate over the time range of calculations.

3. RESULTS AND DISCUSSION

In this section, we will first verify the method of solution and the accuracy of the numerical scheme and will then present results for three values of Reynolds number $Ra = 900$, $Re = 1000$, 5000, where Ra is the Reynolds number based on the length of major axis of the elliptical cross-section and defined by $Ra = U(2a)/v$. In the case of $Re = 5000$, the problem is solved for the five angles of incidence of $\alpha = 0$, 15, 30, 45 and 90°, while the aspect ratio of the ellipse is kept unchanged at $\bar{r} = 0.6$. On the other hand, at $Re = 1000$, the problem is solved for the two angles of incidence of 0 and 30° while keeping the aspect ratio of the ellipse unchanged ($\bar{r} = 0.6$). The Reynolds number case of $Ra = 900$ is only investigated for $\alpha = 45°$ and $\bar{r} = 0.5$. The results are presented in the form of the time variation of the streamline patterns as well as the variations of the drag and lift coefficients and pressure distributions. The variations of the vorticity at small values of time are also presented and compared with a semi-analytical small time-series solution obtained by Staniforth [3]. The computations are terminated at $\tau = 10$ for the cases of $Re = 1000$ and at $\tau = 5$ for the cases of $Re = 5000$. In the case of $Ra = 900$, the computations are carried out only for values of the time up to $\tau = 7$.

The fluid forces acting on the cylinder are mainly the drag and lift forces (D, L) shown in Figure 1. These forces arise from the fluid pressure and shear forces acting on the cylinder surface. We will first obtain an expression for the pressure distribution and then use it to calculate the drag and lift force coefficients. We now introduce the dimensionless pressure coefficient p^* defined by

$$p^*(\eta, t) = \frac{p_\eta - p_\pi}{\frac{1}{2}\varrho U^2}$$

An expression for the surface pressure gradient can be obtained by applying the Navier–Stokes equations at the cylinder surface and making use of the boundary conditions given in (6a)–(6c). After making necessary simplifications, we obtain

$$\left[\frac{\partial p^*}{\partial \eta}\right]_{\xi = \xi_0} = -\frac{4}{Re}\left(\frac{\partial \zeta}{\partial \xi}\right)_{\xi = \xi_0}$$

By using expression (7b) for ζ and integrating both sides of the above expression with respect to η between the two limits of π and η, we obtain

$$p^*(\eta, t) = -\frac{4}{Re}\left\{\frac{1}{2}\frac{\partial G_0}{\partial \xi}(\eta - \pi) + \sum_{n=1}^{N}\frac{1}{n}\left[\frac{\partial G_n}{\partial \xi}\sin n\eta - \frac{\partial g_n}{\partial \xi}(\cos n\eta - \cos n\pi)\right]\right\} \tag{20}$$

The periodicity of p requires that $(\partial G_0/\partial \xi)_{\xi_0}$ must vanish at all times. One can easily prove that the use of the integral condition (18a) is sufficient for satisfying the periodicity of p.

The drag and lift forces can be calculated by considering the components of pressure and shear forces acting on an elementary surface area in the x- and y-directions. The resulting

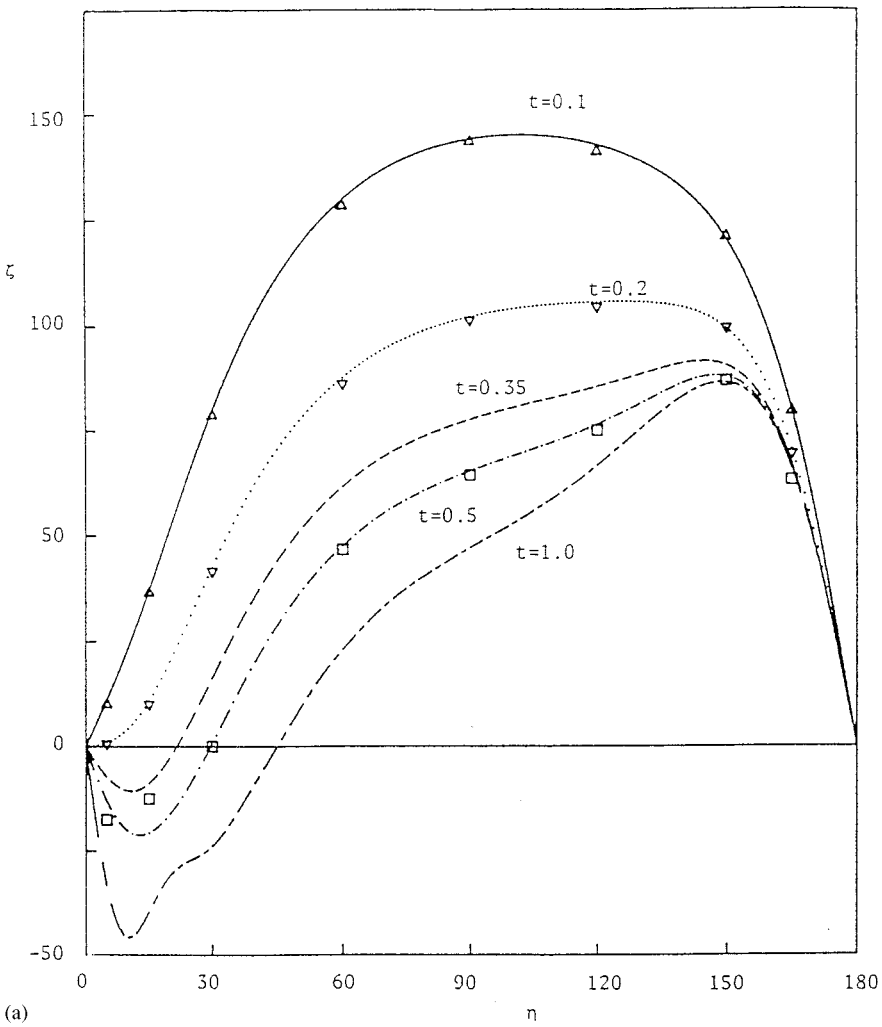

Figure 2. Comparison between the vorticity distribution obtained from the present study and that obtained by Staniforth using a series solution $Re = 5000$, $\bar{r} = 0.6$: (a) $\alpha = 0°$, (b) $\alpha = 15°$, (c) $\alpha = 30°$, (d) $\alpha = 45°$, (e) $\alpha = 90°$.

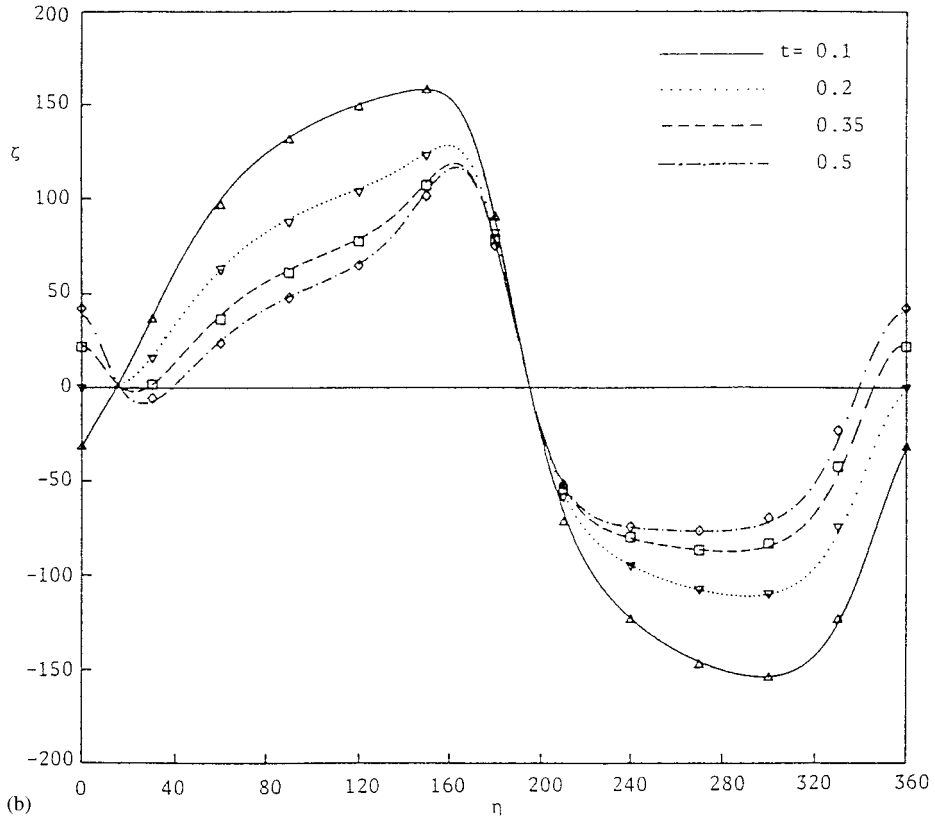

Figure 2 (*Continued*)

equations are integrated around the cylinder surface to obtain expressions for the x- and y-components of fluid forces in terms of the Fourier functions. These can be written as

$$F_{xf} = \pi\mu U \cosh \xi_0 g_1(\xi_0, t)$$

$$F_{yf} = -\pi\mu U \sinh \xi_0 G_1(\xi_0, t)$$

$$F_{xp} = -\pi\mu U \sinh \xi_0 [\partial g_1(\xi, t)/\partial\xi]_{\xi_0}$$

$$F_{yp} = \pi\mu U \cosh \xi_0 [\partial G_1(\xi, t)/\partial\xi]_{\xi_0}$$

where F_{xf} and F_{yf} represent the x- and y-components of the friction forces acting on the cylinder surface, and F_{xp} and F_{yp} are the corresponding components of the pressure forces. The

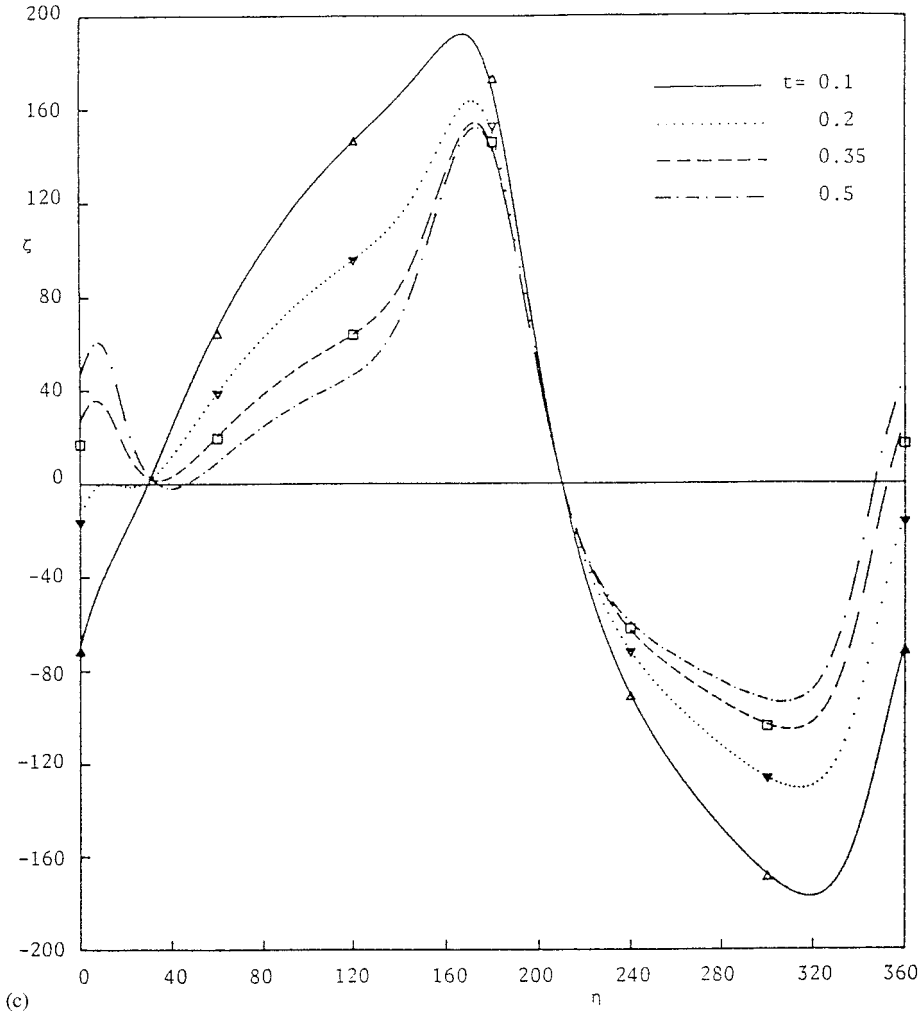

Figure 2. (*Continued*)

contribution of these forces in the horizontal and vertical directions results in the drag and lift forces, D and L, which can be expressed as

$$D = (F_{xf} + F_{xp}) \cos \alpha + (F_{yf} + F_{yp}) \sin \alpha$$

$$L = (F_{yf} + F_{yp}) \cos \alpha - (F_{xf} + F_{xp}) \sin \alpha$$

The drag and transverse force coefficients C_{D} and C_{L} are defined by

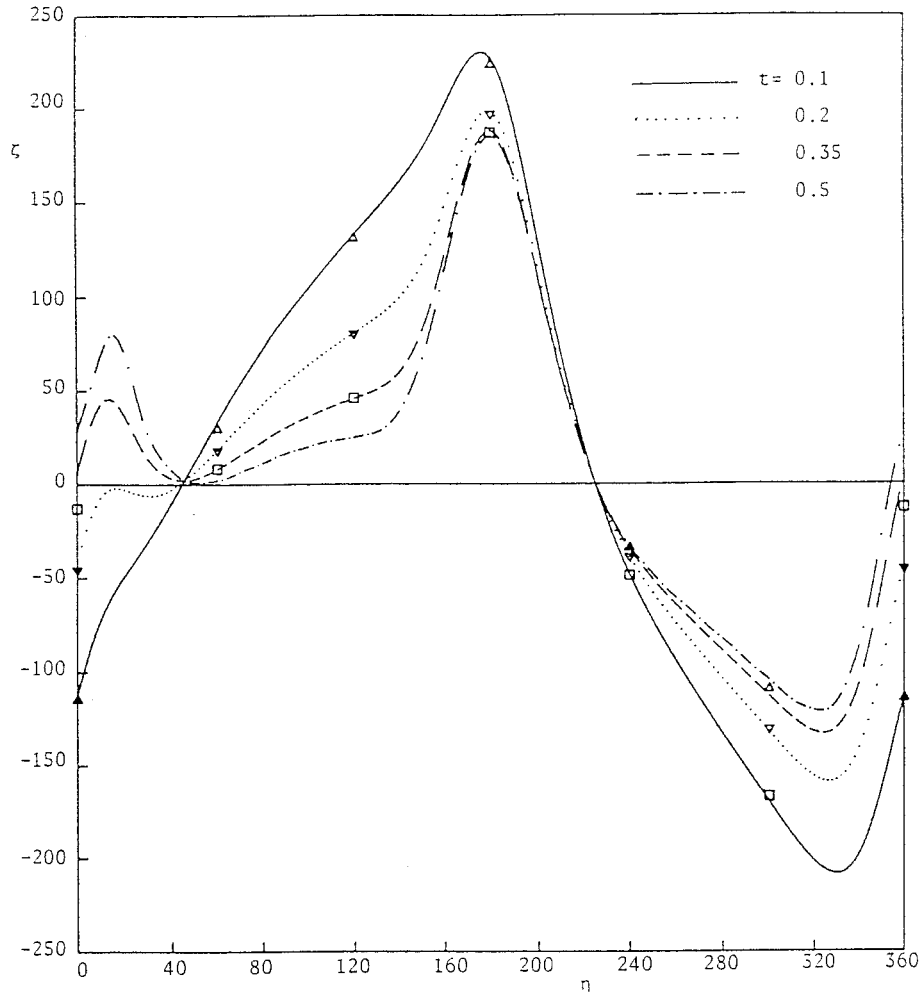

(d)

Figure 2 (*Continued*)

$$C_{\mathrm{D}} = \frac{D}{\frac{1}{2}\varrho U^2(2a)}, \qquad C_{\mathrm{L}} = \frac{L}{\frac{1}{2}\varrho U^2(2a)}$$

The above expression can be split into two parts, one due to frictional forces and the other due to pressure forces. The resulting coefficients can be expressed in terms of the Fourier functions as

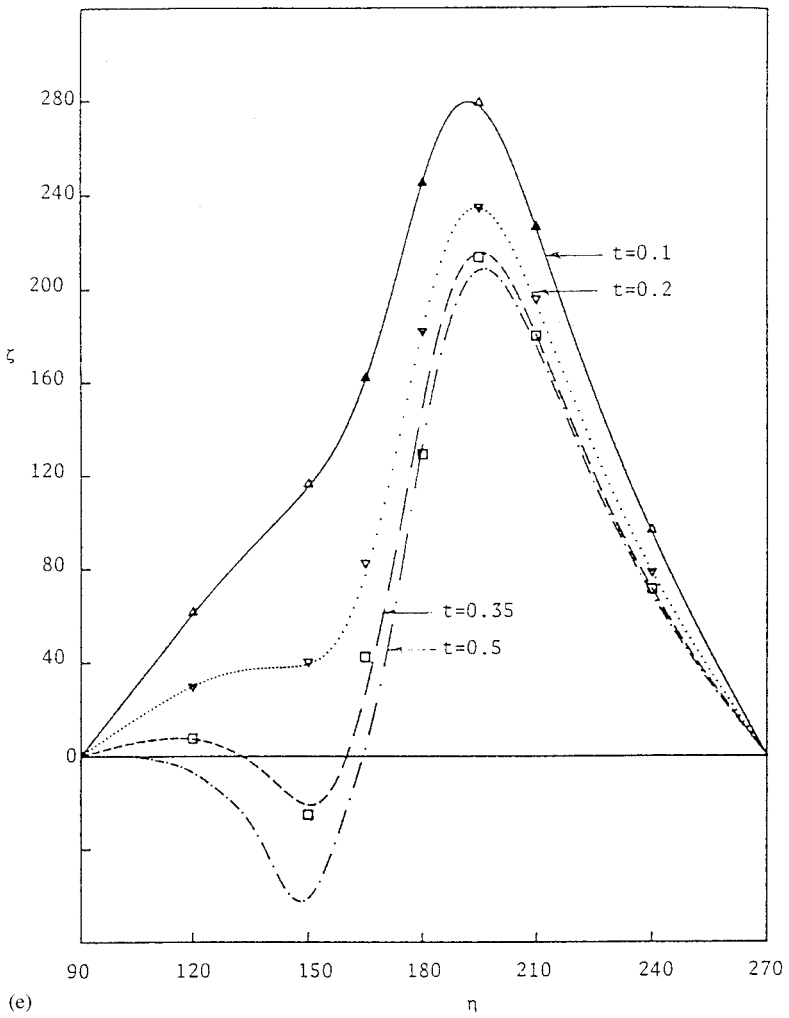

Figure 2 (*Continued*)

$$C_{\mathrm{DF}} = \frac{2\pi}{Re}\,[g_1 \cos\alpha - G_1 \tanh\xi_0 \sin\alpha]_{\xi_0}$$

$$C_{\mathrm{DP}} = \frac{2\pi}{Re}\left[\frac{\partial G_1}{\partial \xi}\sin\alpha - \frac{\partial g_1}{\partial \xi}\tanh\xi_0 \cos\alpha\right]_{\xi_0}$$

$$C_{\mathrm{LF}} = -\frac{2\pi}{Re}\,[g_1 \sin\alpha + G_1 \tanh\xi_0 \cos\alpha]_{\xi_0}$$

$$C_{\mathrm{LP}} = \frac{2\pi}{Re}\left[\frac{\partial G_1}{\partial \xi}\cos\alpha + \frac{\partial g_1}{\partial \xi}\tanh\xi_0 \sin\alpha\right]_{\xi_0}$$

where C_{DF} and C_{DP} are the friction and pressure components of the drag coefficient ($C_{\mathrm{D}} = C_{\mathrm{DF}} + C_{\mathrm{DP}}$) and C_{LF} and C_{LP} are the friction and pressure components of the lift coefficient ($C_{\mathrm{L}} = C_{\mathrm{LF}} + C_{\mathrm{LP}}$).

In order to verify the method of solution and the numerical scheme used in this work, the initial flow for the problem under consideration is calculated. This initial flow was studied analytically by Staniforth [3] who obtained a time-series solution for the stream function and vorticity. However, Staniforth's solution is only valid for a very small time after the start of the cylinder motion. The cases considered for comparison are the cases of $Re = 5000$ when $\bar{r} = 0.6$ and $\alpha = 0$, 15, 30, 45 and 90°. Figure 2(a)–(e) shows comparisons between the surface vorticity distributions obtained from the present study and that obtained by Staniforth using a series solution at small times. These figures show an excellent agreement between the two solutions. Numerical values of the vorticity at various positions are shown in Table I when $\tau = 0.4$, which

Table I. Comparison between the present work and Staniforth's results[a].

Angle (°)	Present	Staniforth (series)	Staniforth (numerical)
0	28.80	28.6	28.8
15	2.20	2.5	2.1
30	−1.86	−0.7	−2.1
45	15.56	15.6	15.3
60	33.67	33.5	33.5
75	47.31	47.0	47.1
90	57.28	56.9	57.0
105	65.34	65.0	65.1
120	73.78	73.4	73.6
135	86.50	86.2	86.4
150	106.60	106.4	106.3
165	117.30	116.2	116.7
180	77.40	77.2	76.9
195	−0.011	−0.2	0.0
210	−51.84	−51.5	−51.6
225	−71.56	−71.2	−71.3
240	−78.08	−77.6	−77.8
255	−81.00	−80.5	−80.7
270	−82.70	−82.2	−82.4
285	−82.92	−82.5	−82.6
300	−79.73	−79.2	−79.5
315	−68.32	−67.6	−68.1
330	−39.71	−37.9	−39.3
345	5.81	2.1	6.8
360	28.80	28.6	28.8

[a] Vorticity variation at $\tau = 0.4$: $Re = 5000$, $\alpha = 15°$ and $\bar{r} = 0.6$.

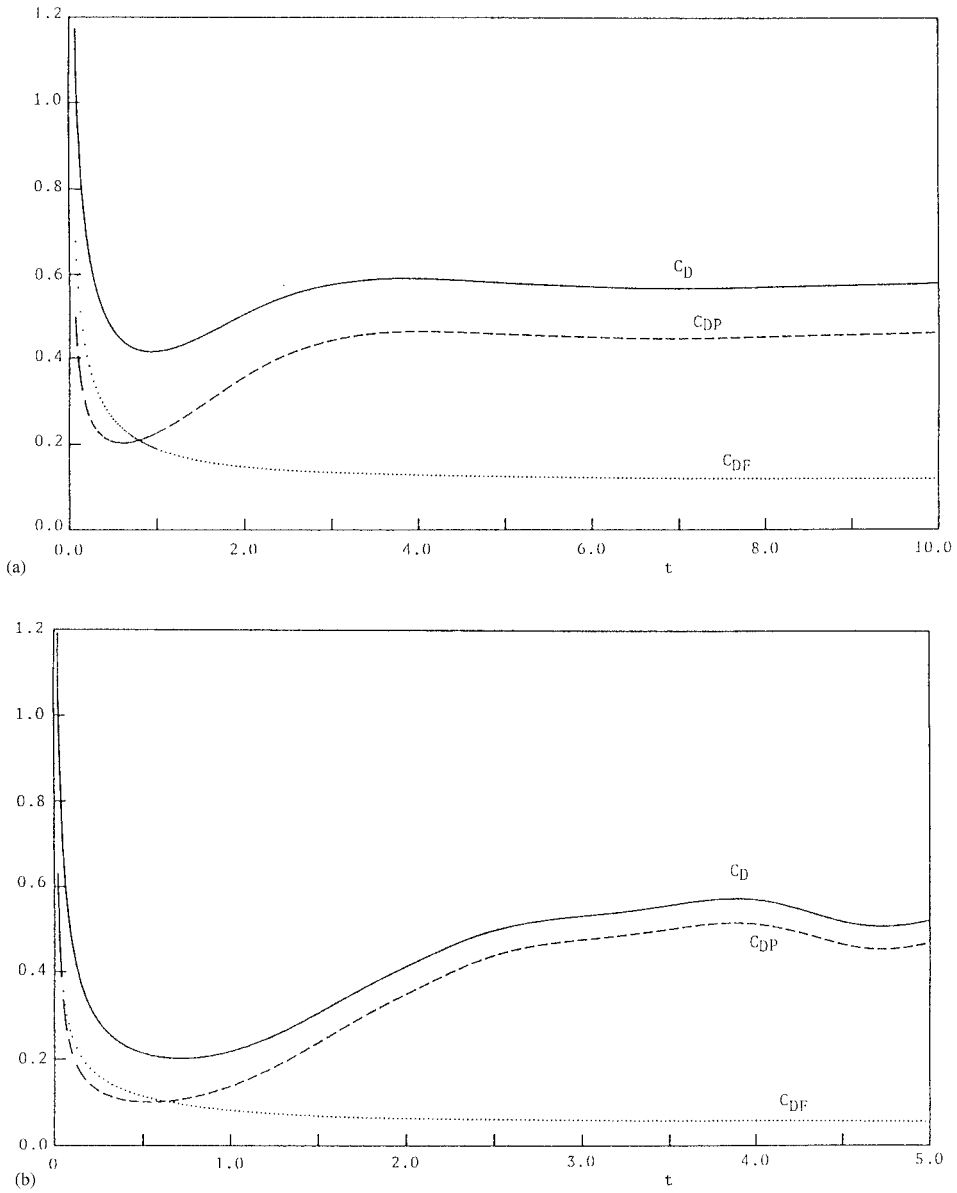

Figure 3. (a) Variation of the drag coefficients: C_{DF}, C_{DP} and C_D with τ at $Re = 1000$, $\bar{r} = 0.6$, and $\alpha = 0°$. (b) Variation of the drag coefficients: C_{DF}, C_{DP} and C_D with τ at $Re = 5000$, $\bar{r} = 0.6$, and $\alpha = 0$.

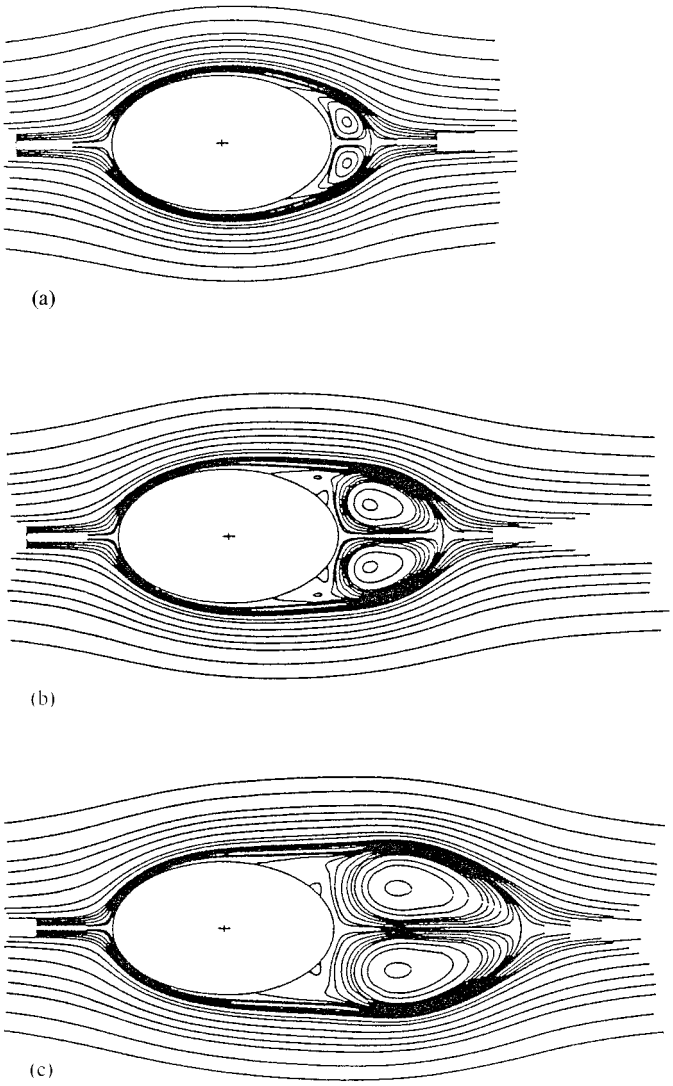

Figure 4. Instantaneous streamlines of the flow for $Re = 1000$, $\bar{r} = 0.6$, and $\alpha = 0°$: (a) $\tau = 2.0$, (b) $\tau = 5.0$, (c) $\tau = 10.0$.

compares the present results with the results of Staniforth in the case of $Re = 5000$, $\alpha = 15°$ and $\bar{r} = 0.6$.

The calculated values of C_{DF}, C_{DP} and C_D when the flow is symmetric about the major axis ($\alpha = 0$) are plotted in Figure 3(a) and (b) for the cases of $Re = 1000$ and 5000 respectively when $\bar{r} = 0.6$. These figures show that the contribution of frictional force to the total drag coefficient

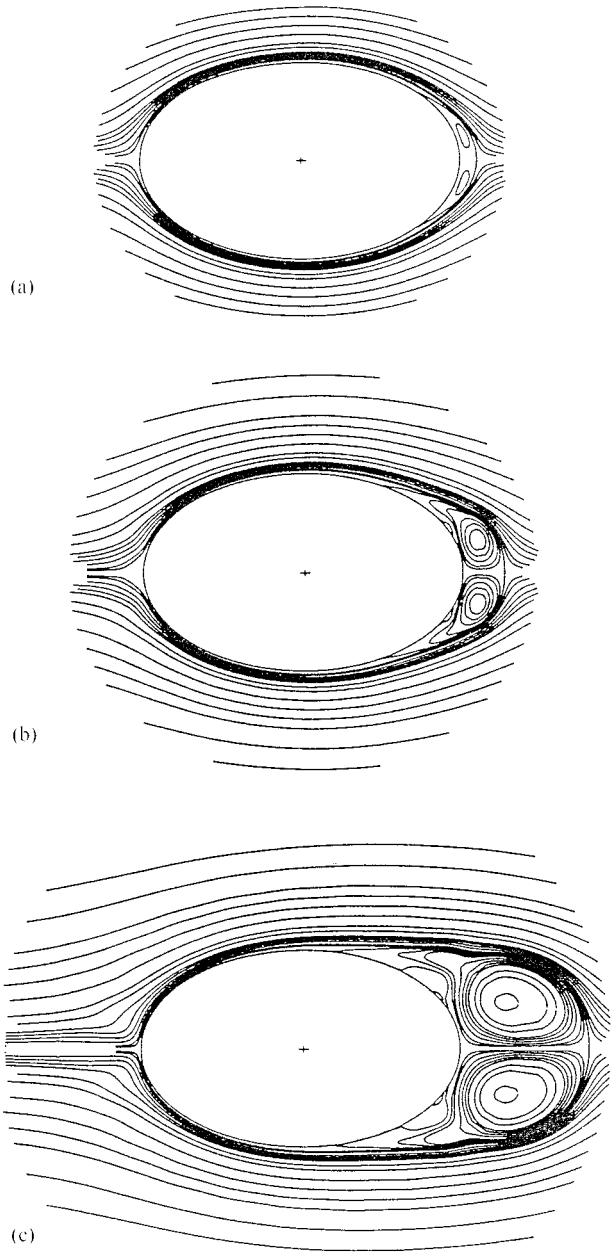

Figure 5. Instantaneous streamlines of the flow for $Re = 5000$, $\bar{r} = 0.6$, and $\alpha = 0°$: (a) $\tau = 1.0$, (b) $\tau = 2.0$, (c) $\tau = 5.0$.

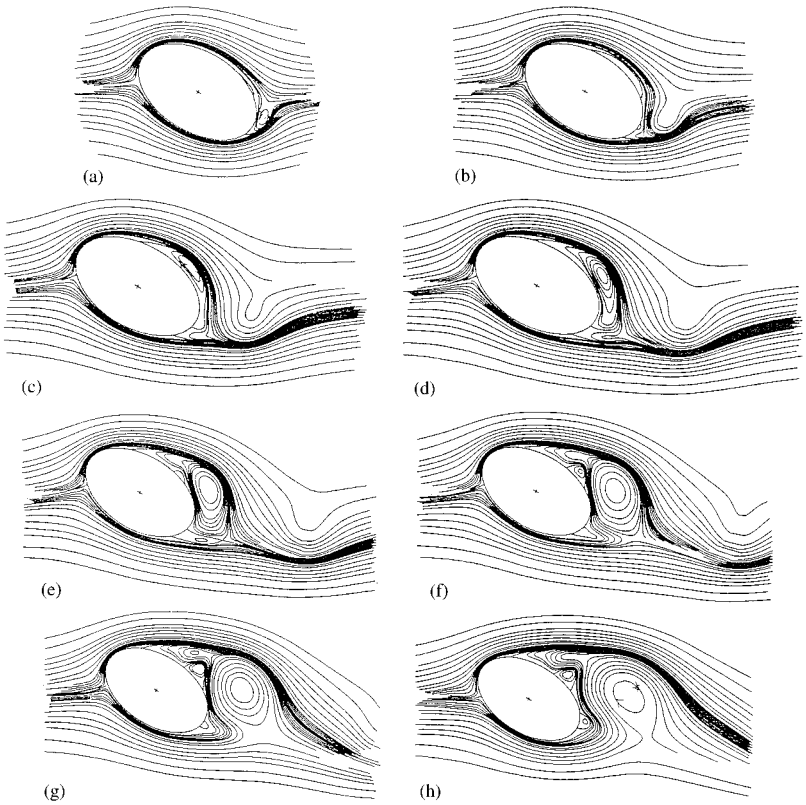

Figure 6. Instantaneous streamlines of the flow for $Re = 1000$, $\bar{r} = 0.6$, and $\alpha = 30°$: (a) $\tau = 1.0$, (b) $\tau = 2.0$, (c) $\tau = 3.0$, (d) $\tau = 4.0$, (e) $\tau = 5.0$, (f) $\tau = 6.0$, (g) $\tau = 7.0$, (h) $\tau = 8.0$, (i) $\tau = 10.0$.

C_D is relatively small. They also show, as expected, that the frictional drag coefficient decreases with the increase of Re. In the case when $Re = 1000$, C_D takes the constant value near 0.6, whereas in the case of $Re = 5000$, C_D becomes periodic after a transition period when $\tau > 4.0$. The instantaneous streamline patterns are plotted for the same two cases ($Re = 1000$ and 5000) when the flow is symmetric about the major axis. The time variation of the streamline patterns is shown in Figure 4(a)–(c) for the first case when τ varies from 2.0 to 10.0 and for the second case in Figure 5(a)–(c) when τ varies from 1.0 to 5.0 respectively. In these figures the usual formations and detachments of upper (clockwise) and lower (counterclockwise) vortex pairs take place.

Nine snapshots of the flow field for the case of $\alpha = 30°$ and $\bar{r} = 0.6$ are shown in Figure 6 when $Re = 10^3$. Figure 6(a) shows the formation of a separation bubble. The vortex resulting from this separation bubble develops at time $\tau = 3.0$ near the upper half of the cylinder. After

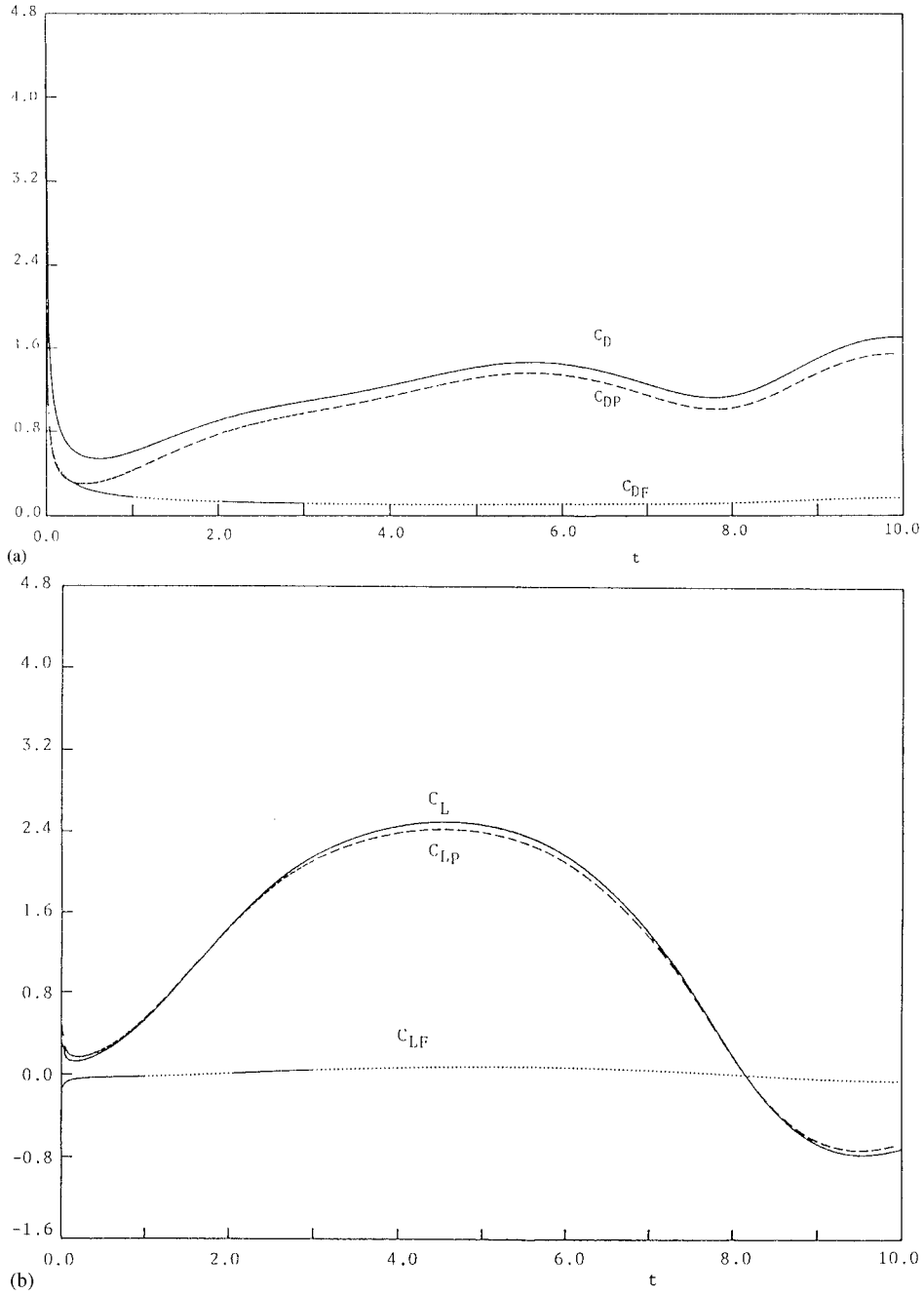

Figure 7. (a) Variation of the drag coefficients: C_{DF}, C_{DP} and C_D with τ at $Re = 1000$, $\bar{r} = 0.6$, and $\alpha = 30°$. (b) Variation of the lift coefficients: C_{LF}, C_{LP} and C_L with τ at $Re = 1000$, $\bar{r} = 0.6$, and $\alpha = 30°$.

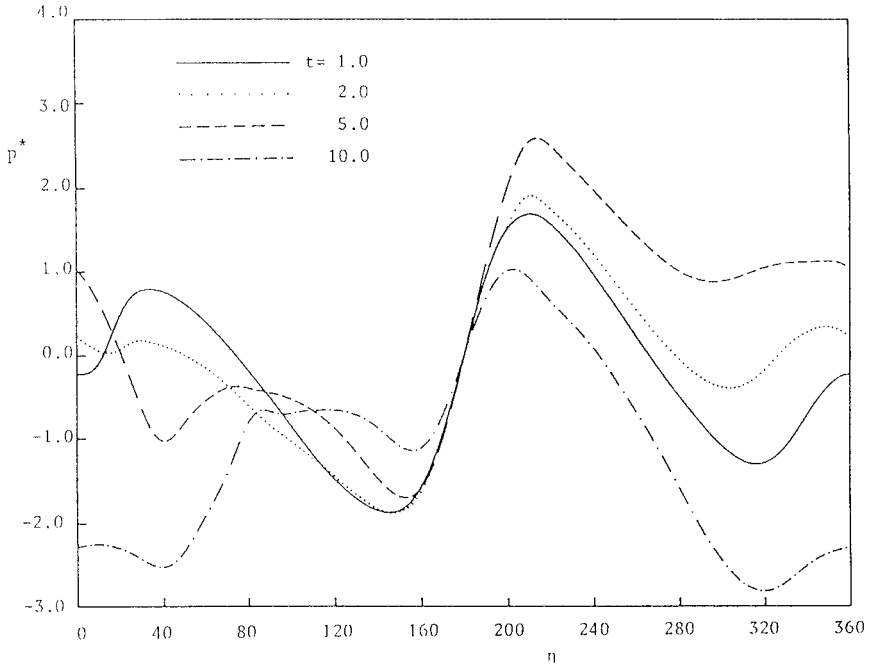

Figure 8. The time development of pressure distribution for the case of $Re = 1000$, $\bar{r} = 0.6$, and $\alpha = 30°$.

a while this vortex detaches and moves downstream. During the time interval $1.0 < \tau < 10.0$, the formations and detachments of upper (clockwise) and lower (counterclockwise) vortex pairs take place and this classical mode of vortex shedding leads to the formation of a Karman street (see Figure 6(i)). Comparison of these figures with the corresponding ones in the case of $\alpha = 0$ indicates that the separation point moves more toward the front of the cylinder as α increases from 0 to 30°, as expected.

In the case of flow past an inclined elliptic cylinder ($\alpha \neq 0$), lift is present unlike the symmetrical case ($\alpha = 0$). The calculated values of C_D and C_L are plotted in Figure 7(a) and (b) respectively for the case of $\alpha = 30°$ and $\bar{r} = 0.6$. These figures indicate periodic variation of the flow field associated with vortex shedding. Comparison of C_D with the corresponding one in the case of $\alpha = 0$ indicates that the C_D curve shows non-periodic behavior in the case $\alpha = 0$, whereas in the case of $\alpha = 30°$, the C_D curve shows a periodic behavior after a transition period when $\tau = 6.0$. Figure 7(b) illustrates an interesting behavior of the lift coefficient, C_L, where it takes negative values after $\tau = 8.0$. It may be noted that this unusual behavior of a negative lift was reported by Taneda [11,12] experimentally (see Taneda [12: p. 295, figures 12 and 14]) but not reported theoretically in any previous work. In order to explain this phenomenon, we relied on the streamline patterns given in Figure 6 together with the time variation of C_L given in Figure 7(b). The decrease in C_L started approximately at $\tau = 5$, which marks the beginning

of detachment of the first vortex and the formation of the second vortex at the upper surface of the cylinder as shown in Figure 6(e). The process of the first vortex detachment continued until $\tau = 7$ (Figure 6(g)). At $\tau = 8$, the first vortex started shedding away from the surface (Figure 6(h)) causing a net circulation in the reverse direction and resulting in the negative lift. This phenomenon represents a new contribution of this work. Figure 8

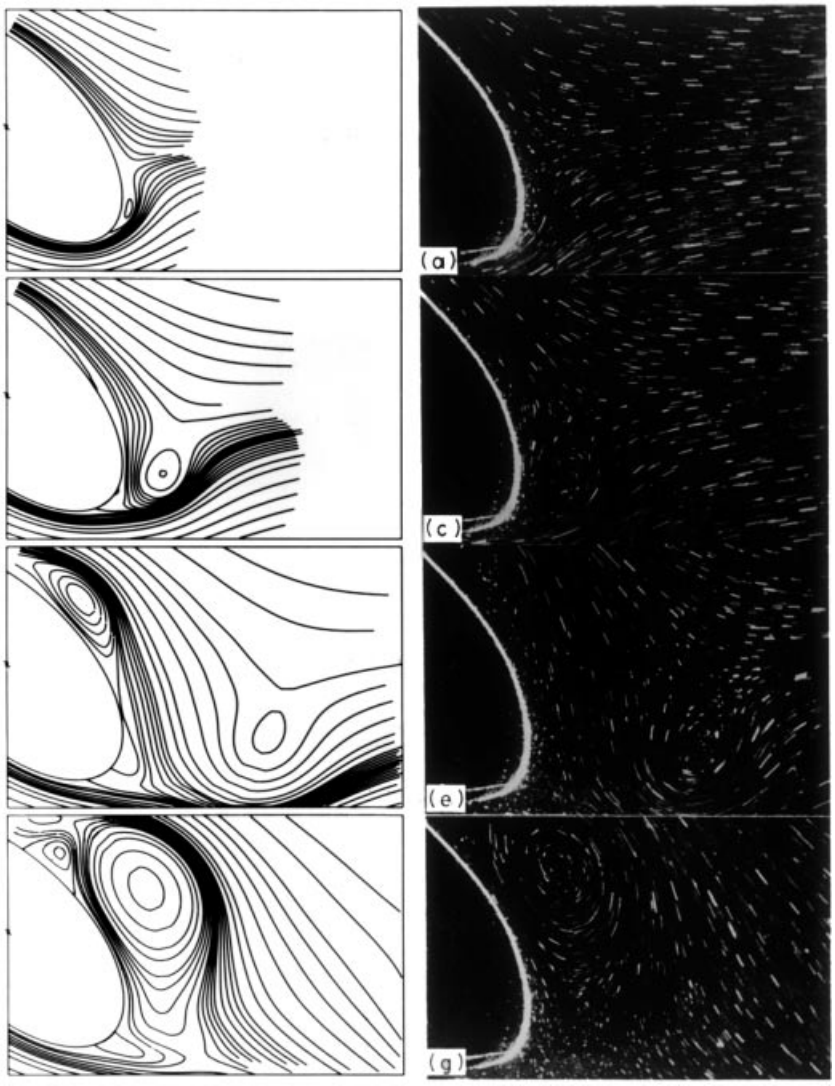

Figure 9. Comparison with Taneda's flow visualization for $Ra = 900$, $\bar{r} = 0.6$, and $\alpha = 45°$: (a) $\tau = 0.416$, (b) $\tau = 0.808$, (c) $\tau = 1.224$, (d) $\tau = 1.917$, (e) $\tau = 2.702$, (f) $\tau = 3.856$, (g) $\tau = 4.942$, (h) $\tau = 7.020$.

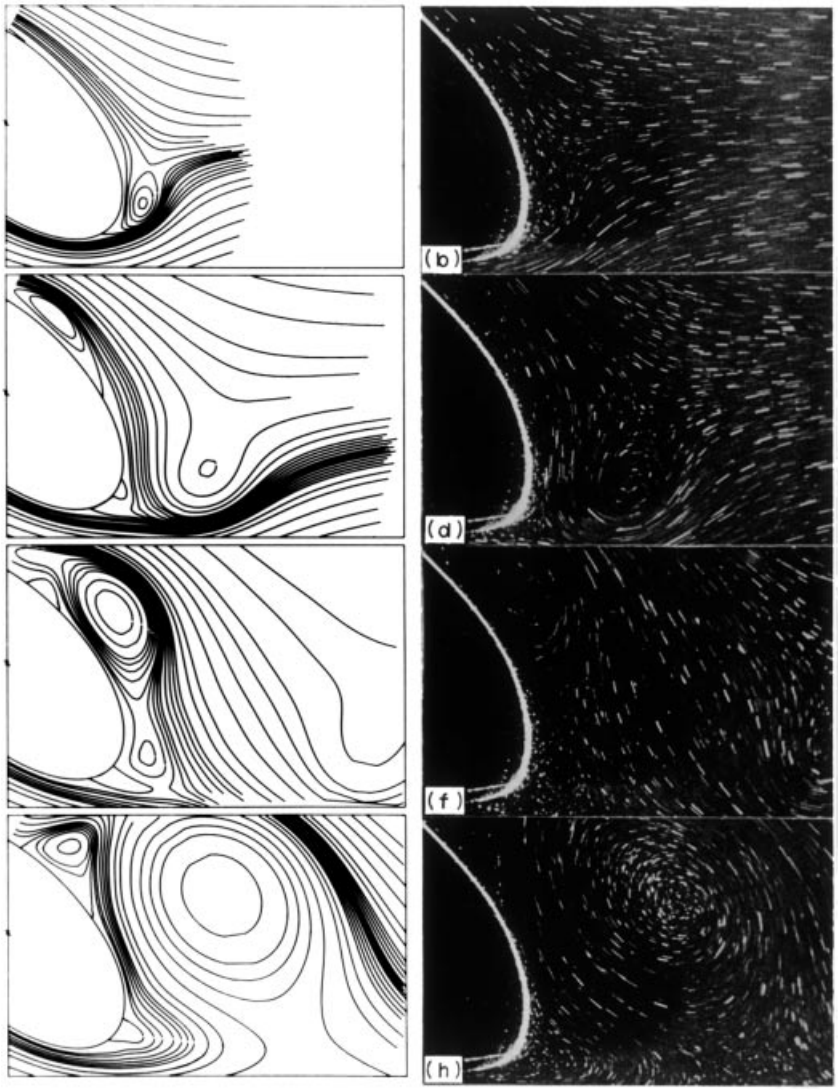

Figure 9 (*Continued*)

shows the time variation of the surface pressure distribution for the same case at $\tau = 1.0$, 2.0, 5.0, 10.0.

In order to compare the obtained streamline patterns with the experimental flow visualization reported by Taneda [12], the case of $\alpha = 45°$, $\bar{r} = 0.5$, when $Ra = 900$ was investigated. Figure 9 shows a comparison between the present results at eight time steps and those reported

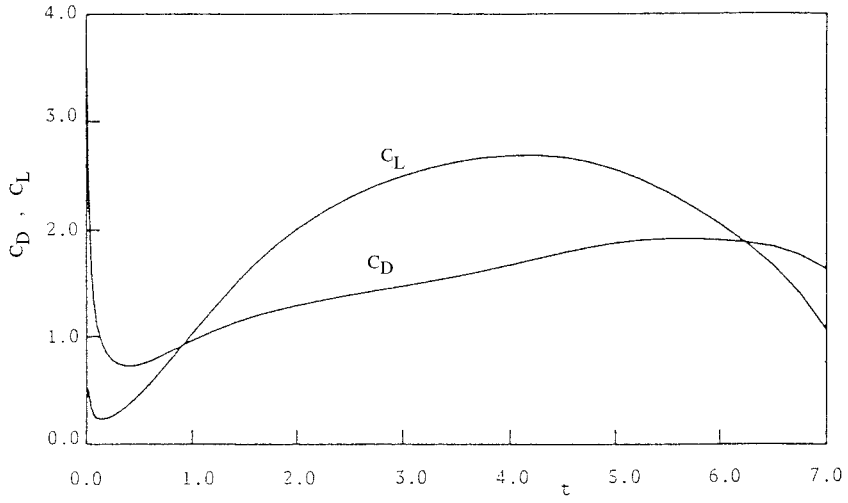

Figure 10. Variation of the total drag and lift coefficients with τ at $Ra = 900$, $\bar{r} = 0.6$, and $\alpha = 30°$.

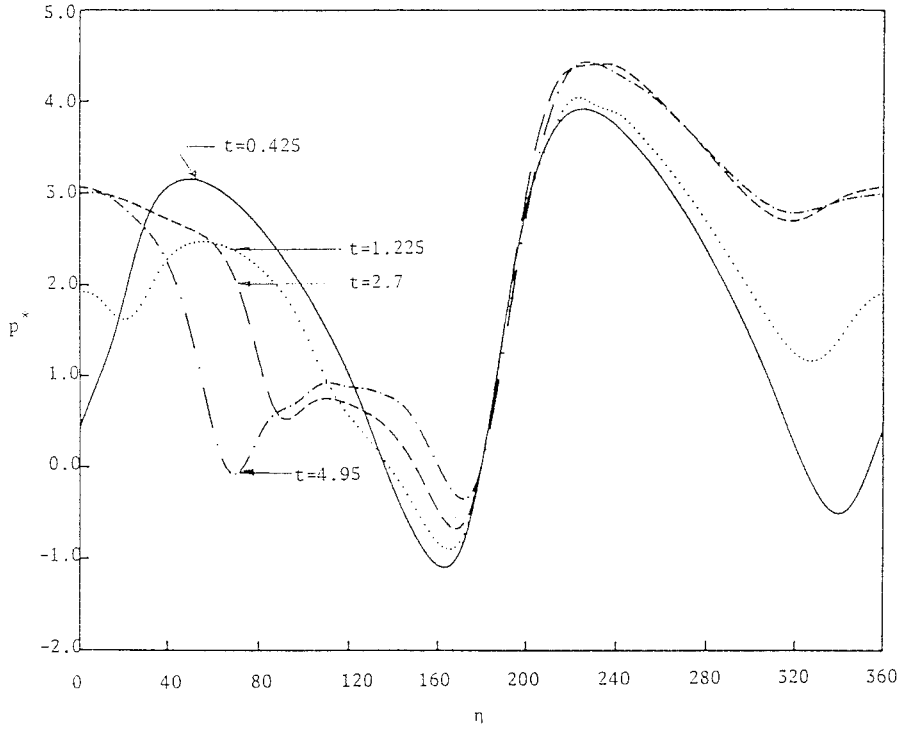

Figure 11. The time development of pressure distribution for the case of $Ra = 900$, $\bar{r} = 0.6$, and $\alpha = 45°$.

by Taneda [12] where an excellent agreement was found. The time variations of the drag and lift coefficients are shown in Figure 10. Figure 11 shows the time variation of the surface pressure distribution for the same case at $\tau = 0.425$, 1.225, 2.7 and 4.95.

4. CONCLUSIONS

In the present paper we have considered the initial phase of flow development past an inclined elliptic cylinder. The study is based on a numerical integration of the Helmoltz vorticity transport equation together with the stream function equation. A boundary layer co-ordinate system was used following the start of fluid motion to ensure high accuracy at small times. Integral conditions were deduced and used in the numerical scheme for accurate prediction of the vorticity components at the solid boundary and also to ensure that the pressure is single valued at any point around the cylinder surface. Various comparisons are made with previous theoretical and experimental results including flow visualizations to validate the solution methodology and an excellent agreement was found. The numerical solution was carried out sufficiently far in time to reveal an interesting transient phenomenon of negative lift occurring shortly after the start of motion for a positive angle of attack. This is the first time this phenomenon has been reported theoretically.

ACKNOWLEDGMENTS

The support received from King Fahd University of Petroleum and Minerals as well as the Natural Sciences and Engineering Council of Canada is gratefully acknowledged.

REFERENCES

1. Wang C-Y. Separation and stall of an impulsively started elliptic cylinder. *ASME Journal of Applied Mechanics* 1967; **34**: 823–828.
2. Dennis SCR, Staniforth AN. A numerical method for calculating the initial flow past a cylinder in a viscous fluid. In *Proceedings of the 2nd International Conference Numerical Methods in Fluid Dynamics*, *Lecture Notes in Physics*, vol. 8, Holt M (ed.). Springer-Verlag: Berlin, 1971; 343–349.
3. Staniforth AN. Studies of symmetrical and antisymmetrical viscous flows past impulsively started cylinders. PhD thesis, The University of Western Ontario, London, Canada, 1972.
4. Panniker PKG, Lavan Z. Flow past impulsively started bodies using Green's functions. *Journal of Computational Physics* 1975; **18**: 46–65.
5. Howarth L. Note on the development of the circulation around a thin elliptic cylinder. *Proceedings of Cambridge Philosophical Society* 1939; **31**: 528.
6. Dennis SCR, Kocabiyik S. An asymptotic matching condition for unsteady boundary-layer flows governed by the Navier–Stokes equations. *IMA Journal of Applied Mathematics* 1991; **47**: 81–98.
7. Lugt HJ, Haussling HJ. Laminar flow past an abruptly accelerated elliptic cylinder at 45° incidence. *Journal of Fluid Mechanics* 1974; **65**: 711–734.
8. Honji H. Starting flows past spheres and elliptic cylinders. Reports of the Research Institute of Applied Mechanics, Kyushu University, Japan, Vol. XIX, No. 65, 1972.
9. Patel VA. Flow around the impulsively started elliptic cylinder at various angles of attack. *Computers and Fluids* 1981; **9**: 435–462.
10. Nair MT, Sengupta TK. Unsteady flow past elliptic cylinders. *Journal of Fluids and Structures* 1997; **11**: 555–595.
11. Taneda S. The development of the lift of an impulsively started elliptic cylinder at incidence. *Journal of the Physics Society of Japan* 1972; **33**: 1706–1711.

12. Taneda S. Visual study of unsteady separated flows around bodies. *Progress in Aerospace Science* 1977; **17**: 287–348.
13. Badr HM, Dennis SCR. Time-dependent viscous flow past an impulsively started rotating and translating circular cylinder. *Journal of Fluid Mechanics* 1985; **158**: 447–488.
14. Badr HM, Coutancean M, Dennis SCR, Menard C. Unsteady flow past a rotating circular cylinder at Reynolds numbers 10^3 and 10^4. *Journal of Fluid Mechanics* 1990; **220**: 459–484.